JGR Oceans

RESEARCH ARTICLE
10.1029/2019JC015879

Observations of the Low-Mode Internal Tide and Its Interaction With Mesoscale Flow South of the Azores

Jonas Löb[1,2], Janna Köhler[1,2], Christian Mertens[2], Maren Walter[1,2], Zhuhua Li[3], Jin-Song von Storch[3,4], Zhongxiang Zhao[5], and Monika Rhein[1,2]

[1]MARUM – Center for Marine Environmental Science, University of Bremen, Bremen, Germany, [2]Institute of Environmental Physics, University of Bremen, Bremen, Germany, [3]Max Planck Institute for Meteorology, Hamburg, Germany, [4]Center for Earth System Research and Sustainability (CEN), University of Hamburg, Hamburg, Germany, [5]Applied Physics Laboratory, University of Washington, Seattle, WA, USA

Key Points:

- Mean energy flux of 11.1 kW m^{-1} during a quiet period reduces to 7.2 kW m^{-1} during a period of interaction with a surface intensified eddy
- The coherent part of the energy flux is reduced by more than 40% during a surface eddy period in comparison to a no-eddy period
- The observed energy flux correlates reasonably well with output from satellite altimetry and a global high-resolution ocean circulation model

Correspondence to:
J. Löb,
jloeb@uni-bremen.de

Citation:
Löb, J., Köhler, J., Mertens, C., Walter, M., Li, Z., von Storch, J.-S., et al. (2020). Observations of the low-mode internal tide and its interaction with mesoscale flow south of the Azores. *Journal of Geophysical Research: Oceans*, *125*, e2019JC015879. https://doi.org/10.1029/2019JC015879

Received 19 NOV 2019
Accepted 24 OCT 2020

Abstract Understanding the temporal variability of internal tides plays a crucial role in identifying sources and sinks of energy in the ocean. Using a 10-month-long time series from moored instruments inside a tidal beam south of the Azores, the magnitude and the underlying causes of temporal variability in the first two modes of the internal tide energy flux was studied. We analyzed changes of the direction and coherence of the energy flux, its modal structure, and the impact of two eddies. Semidiurnal energy fluxes were further compared with estimates from a 1/10° ocean global circulation model, as well as with fluxes derived from satellite altimetry. All energy fluxes correlate reasonably well in direction, deviations from its fixed phase relation to astronomical forcing, and modal composition while model and satellite underestimate the total energy flux. A pronounced damping of the in situ fluxes coincides with the passing of two eddies. In the presence of a surface-intensified eddy, the coherent part of the energy flux in the first two modes is lowered by more than 40%, a subsurface eddy coincides with a decrease of the energy flux mainly in the second mode. These observations support the hypothesis that eddy interactions increase the incoherent part of the energy flux and transfer energy from low modes into higher modes, which can lead to increased local dissipation. It remains an open question how much of the energy converted from lower to higher modes results in local dissipation, a crucial part in creating energetically consistent ocean-climate models.

Plain Language Summary Internal tides are generated when a tidal wave interacts with underwater obstacles. These waves inside the water column transport energy throughout the ocean until they break and mix the water. Because this mixing is important for the ocean circulation and our climate, it is necessary that we understand all aspects of their behavior. In this study, we use year-long observations of internal tides and their energy in a region south of the Azores Islands in the northeast Atlantic, where they are particularly strong. We compare our measurements with results from satellites and a global ocean circulation model and analyze the influence of eddies on internal tide energy. Eddies are common large-scale vortices in the ocean which can make internal tides dissipate locally, hence making their energy available for local mixing. Our measurements show a decrease in energy flux by about one third when eddies interact with internal tides.

1. Introduction

The breaking of internal waves results in diapycnal mixing which plays an important role in different climate relevant processes such as the transport of heat, freshwater, nutrients, pollutants, and dissolved gases. Thus, it is necessary to study the physics that drives diapycnal mixing to adequately represent the ocean's role in the climate system and to construct realistic climate models. Approximately 2 TW are needed to maintain the abyssal stratification of which internal tides contribute the main share, about 0.5–1.5 TW (Munk & Wunsch, 1998; Nycander, 2005; Waterhouse et al., 2014; Wunsch & Ferrari, 2004). Internal gravity waves occur everywhere in the stratified ocean and can be grouped in different categories depending on their generation mechanism. Here, we discuss semidiurnal M_2 internal tides generated by the barotropic tides flowing over rough topography. Away from their immediate generation sites, internal waves in the stratified ocean take the form of standing vertical modes (e.g., Anderson & Gill, 1979). The first baroclinic mode is characterized by a reversal of the horizontal flow direction in the depth of the thermocline while

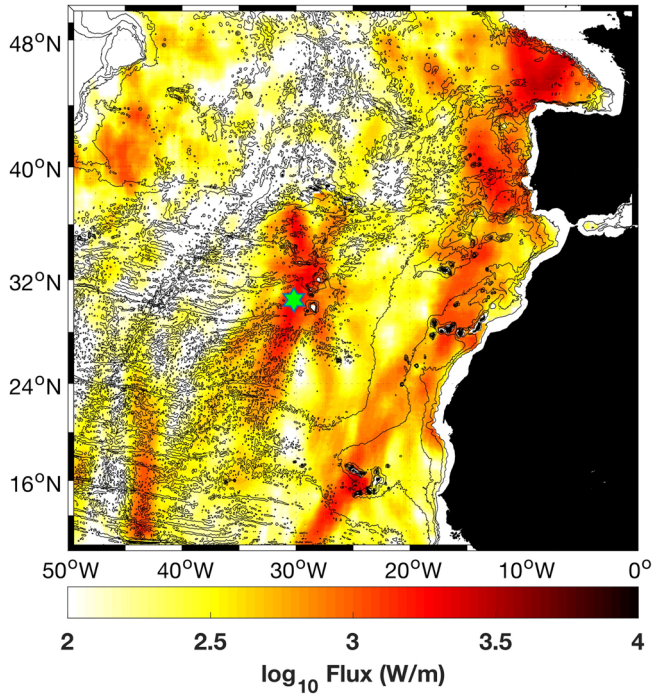

Figure 1. Mode 1 energy flux from satellite altimetry with the location of the mooring inside a beam of internal tide energy flux south of the Azores denoted by the green star; black contour lines represent the bathymetry contoured every 1,000 m.

higher modes have a more complicated vertical structure. The phase and group speed of the internal waves decrease with increasing mode number. Low-mode motions contain appreciable energy depending on the spectral characteristics of the generating topography (e.g., de Lavergne et al., 2019) and quickly propagate away laterally up to thousands of kilometers from their generation sites, for example the Hawaiian Ridge (Alford, 2003; Cummins et al., 2001; Dushaw et al., 1995; Nash et al., 2004; Zhao et al., 2016) or the seamount chain south of the Azores (Köhler et al., 2019), our study region (Figure 1). Higher modes contain much of the vertical shear in the ocean (Simmons & Alford, 2012) and dissipate close to their generation region, also owing to their slower group velocities. Internal tides radiate about 20%–80% of their energy away as low-mode internal waves with the remainder being dissipated by near-field tidal mixing (Buijsman et al., 2016; de Lavergne et al., 2019; MacKinnon et al., 2017).

When internal tides radiate away from their generation site, they can transfer energy to waves of other frequencies via wave-wave interactions and ultimately deposit their energy in form of turbulent mixing. Interactions between internal tides, mesoscale eddies, and currents are inevitable because of the large distance that low-mode internal tides are able to propagate. This makes a significant fraction of the internal wavefield unpredictable because these interactions can modify propagation directions, adjust propagation speeds, change the coherent fraction of the energy flux, lead to wave deflection, and increase dissipation (Alford et al., 2012; Kelly & Lermusiaux, 2016; Nash, Kelly, et al., 2012; Nash, Shroyer, et al., 2012). The presence of mesoscale eddies is assumed to be the main driver of temporal variability in the energy contained in the internal wavefield apart from the changes in the energy of the internal tide that are induced by the spring-neap cycle in its forcing (Ponte & Klein, 2015; Whalen et al., 2018; Zaron & Egbert, 2014). Mesoscale eddies often have a barotropic or mode 1 baroclinic vertical structure (McWilliams, 1985) and their length scale, typically in the order of 100 km (Eden, 2007; Krauss et al., 1990) is comparable to that of the low-mode internal tides. This makes them a potential partner for interaction according to the resonant triad theory where the eddy contains energy at the required wave number to complete resonant triads between mode 1 and mode 2 internal tides. The result might be an enhancement of the energy cascade, represented by a downscale transfer of energy into higher modes which increases the local dissipation at the expense of less dissipation at remote locations (Dunphy & Lamb, 2014).

Internal tides imprint a signature on the sea level which is on the order of several centimeters, but do not necessarily maintain a fixed phase relation with the astronomical forcing (Ray & Zaron, 2011; Shriver et al., 2014). Deviations from this phase relation are defined as incoherence. Internal tide incoherence is attributed to both modulations in the stratification at the generation sites (Kelly & Nash, 2010; Zilberman et al., 2011) and interactions between propagating internal tides and background variations of the low-frequency circulation (Chavanne et al., 2010; Rainville & Pinkel, 2006).

The understanding of ocean processes, such as the propagation and dissipation of internal tides, which are often too simply parameterized in numerical ocean models, is necessary to make ocean and climate models energetically more consistent. Up to now ocean models are for the main part not energetically consistent, for example, they produce mixing without considering the amount of kinetic energy available (Eden et al., 2014). The energy flux is an important benchmark for these models because its divergence identifies sources and sinks of energy. It is still a challenge to observe and realistically include internal tides in ocean general circulation models (OGCMs). High-resolution concurrent simulations of circulation and tides have become an important tool to study internal tides in the ocean. This has been done with the 1/12.5° HYCOM model (Arbic et al., 2010, 2012), the MITgcm (Savage et al., 2017), and with the 1/10° MPI-OM (STORMTIDE; Z. Li et al., 2015, 2017; Müller et al., 2012). It is therefore necessary to investigate how

Table 1
Instrument Pairs of Current and Temperature Sensors, Their Depth, Sampling Interval, and Sampling Accuracy Used at Mooring Location 30.48°N, 30.12°W

#	Instrument type	Depth	Sampling interval	Sampling accuracy
1	ADCP	299 m	10 min	±1.2 cm s^{-1}
	SBE56		1 min	±0.002°C
2	Current meter	609 m	10 min	±5 mm s^{-1}
	SBE56		1 min	±0.002°C
3	Current meter	1,027 m	10 min	±5 mm s^{-1}
	SBE56		1 min	±0.002°C
4	Current meter	1,426 m	10 min	±5 mm s^{-1}
	SBE39plus		1 min	±0.002°C
5	Current meter	2,053 m	10 min	±5 mm s^{-1}
	SBE39plus		1 min	±0.002°C
6	Current meter	2,889 m	10 min	±5 mm s^{-1}
	SBE39plus		1 min	±0.002°C
7	Current meter	3,729 m	10 min	±5 mm s^{-1}
	SBE39plus		1 min	±0.002°C
8	Current meter	4,566 m	10 min	±5 mm s^{-1}
	SEB39plus		1 min	±0.002°C

Note. SBE56 and SBE39plus: Temperature loggers. Current meters: Acoustic current meters from Nortek. ADCP: 150 kHz Teledyne RD Instruments Quartermaster.

well such models are able to simulate internal tide energy fluxes (Ansong et al., 2017). Theoretical and idealized studies, as well as in situ studies with a regional focus are the main source of information regarding internal wave energy fluxes and their temporal variability. When comparing point-wise observations with models, the complex interference patterns of baroclinic energy fluxes of multiple waves needs to be considered.

In this study, we investigate the characteristics of the energy flux within a tidal beam south of the Azores using in situ observations and satellite altimetry. The temporal and directional variability of the energy flux of internal tides as well as the variations of its modal composition and its coherence with barotropic forcing are studied and compared to their representation in a state-of-the-art ocean model. We calculated energy flux in the semidiurnal frequency (M_2) from our mooring data as well as in the model STORMTIDE2 following the method described in Alford and Zhao (2007) and Nash et al. (2005). The seamount chain south of the Azores, which has been earlier identified by Köhler et al. (2019) as the generation site for the internal tides, is considered to be one of the main generation sites for internal tides in the North Atlantic (Müller et al., 2012; Zhao et al., 2016). We look at the interactions of one surface and one subsurface intensified eddy present in our observational record with the semidiurnal internal tide energy flux calculated from mooring measurements. Furthermore, we compare how well the global datasets of M_2 internal tide energy fluxes from STORMTIDE2 and satellite altimetry represent the results of our direct in situ measurements.

This work was carried out in the framework of an integrated effort to improve the energy cycle in climate models (DFG CRC181, Energy Transfers in Atmosphere and Ocean). The study is structured as follows: In Section 2, we introduce the data sets and the methods used to derive the energy flux. Thereafter, we present and discuss the temporal and directional variability of the energy flux, the ratio of the individual modes and their coherent—incoherent partitioning in the measured time series in Section 3. In Section 4, we analyze the influence of two eddies on the energy flux, followed by an evaluation on how well the results of the measurements are represented in the STORMTIDE2 model and in results from satellite altimetry in Section 5. A summary of the results and the conclusions are presented in Section 6.

2. Data and Methods

2.1. Mooring Data

A mooring was deployed at 30.48°N and 30.12°W on August 8, 2017 and recovered on May 10, 2018 (Figure 1). The position of the mooring was chosen based on the distributions of M_2 energy flux derived from satellite altimetry (Zhao et al., 2016) and from STORMTIDE model simulations (Müller et al., 2012). The goal was to find a location with a strong tidal signal, a low wind energy input into the mixed layer and a relatively low meso- and submesoscale variability. The mooring was equipped with three Sea-Bird SBE56 temperature loggers, five Sea-Bird SBE39plus temperature loggers, an upward looking 150 kHz Teledyne RD Instruments Quartermaster acoustic doppler current profiler (ADCP), and seven Nortek Aquadopp acoustic current meters. The eight temperature loggers measured with a sampling interval of 1 min, the ADCP and current meters recorded horizontal and vertical velocity with a sampling interval of 10 min. The mooring layout was designed to resolve mode 1 and mode 2 of the internal tide energy flux (Nash et al., 2005). A comprehensive list of all instrument pairs with their corresponding depths, sampling interval, and sampling accuracy is given in Table 1. The ADCP recorded 19 bins with a length of 8 m each. For consistent nonbiased data, the five bins closest to the ADCP were averaged to one data point. The vertical mooring motions were small with a maximum displacement over the deployment period of 43 m, and typical values between 10 and 20 m. The background stratification profile was calculated as the mean of 11 repeated conductivity

temperature depth (CTD) casts close to the mooring location that were measured directly before the mooring deployment during cruise POS516 (Walter et al., 2018). The measured velocity and temperature data are filtered with a fourth-order Butterworth filter with zero-phase response for the semidiurnal component M_2 in the bandwidth $(c^{-1}\omega, c\omega)$, with $c = 1.25$. The semidiurnal frequencies M_2 and S_2 are too close to be separated via band-pass filtering, therefore the filtered variables are expected to show a spring-neap variability. The bandwidth parameter c was chosen narrow enough to maximally isolate the M_2 frequency, while being wide enough to avoid filter ringing (Alford & Zhao, 2007).

2.2. STORMTIDE2 Model Data

An existing run of an internal wave resolving ocean circulation model (1/10°) was used to compare the energy fluxes and their variability found in the in situ observations to the representation in numerical state-of-the-art ocean models. For this, the STORMTIDE2 model was used, a successor of the STORMTIDE simulation (Müller et al., 2012). It is a global high-resolution ocean tide and circulation model with an embedded thermodynamic sea-ice model. STORMTIDE2 is forced by the full lunisolar tidal potential to excite tides, therefore hundreds of tidal constituents are explicitly taken into consideration and the energy flux due to the generated semidiurnal internal tides is expected to show a spring-neap variability. STORMTDE2 has 40 unevenly distributed vertical layers ranging from 10–70 m (in the uppermost 500 m) to 500–600 m (in the deep ocean), and a horizontally nonsymmetric tripolar spherical grid with an almost uniform resolution of 0.1°, that is, about 11 km at the equator and about 9.5 km in the research area. It has two poles in the northern and one in the southern hemisphere. Consequently, the grid size decreases toward the South Pole, whereas it remains more or less uniform north of the equator. A climatological forcing is used as a surface forcing for the spin up period of 33 years until the ocean reaches a quasiequilibrium state. It is then switched to 6-hourly wind forcing (from National Centers for Environmental Prediction) at the ocean surface instead of climatologic wind forcing used in STORMTIDE, including also 6-hourly buoyancy forcing at the surface. The model was integrated for the years 1981–2012. We analyzed 4 months of the model data output of the last simulation year (2012), where we considered 1 month per season, to cover possible seasonal changes, especially in the mixed layer. The stratification profile used as background for the energy flux calculation is the mean stratification over the four analyzed model months. A subsampling of the vertical model layers toward the number of current meters in the mooring is not expected to significantly change the resultant energy flux calculations compared the full resolution (Ansong et al., 2017). The temporal resolution of the output used for our calculation is 1 h. The model is capable of resolving low-mode internal tides: A comparison between the co-tidal charts from STORMTIDE2 and the global tide model TPXO9, as well as between the mean temperature (t) and the stratification profiles (N^2), used for the energy flux calculations from STORMTIDE2 and the in situ observations is shown in Figure 2. TPXO is a series of global models of ocean tides and offers complex amplitudes of sea surface elevations and transport/currents for primary, long period, and nonlinear harmonic constituents. For this comparison, we used the 1/6°-resolution tidal model TPXO9 (Egbert & Erofeeva, 2002). TPXO9 is also later used for the comparison with the spring-neap cycle of M_2 energy fluxes (cf. Figure 4).

In Figures 2a and 2b, one can identify higher amplitudes in the M_2 barotropic tide of STORMTIDE2 compared to TPXO9 at the seamounts south of the Azores, which are strong conversion regions of barotropic to baroclinic energy. The difference between the higher barotropic velocities in STORMTIDE2 compared to TPXO9 is most likely caused by the difference in the spatial resolution of 0.1° and 0.6°, respectively. Especially in regions with rapidly changing and small-scale topography the lower resolution of TPXO9 could underestimate the barotropic velocities. Furthermore, a too weak conversion rate from barotropic to baroclinic energy of STORMTIDE2, together with a too strong dissipation, could lead to an underestimate of the low-mode internal tide energy flux, even when the barotropic tide is strong. The difference in the amplitude between STORMTIDE2 and TPXO9 at the mooring location is about 1.3 cm, which is still a reasonable value for the open ocean in both datasets. The phase of the M_2 barotropic tide is in good agreement with TPXO9. The comparison of the mean temperature and stratification profiles between in situ measurements from CTD and STORMTIDE2 (Figures 2c and 2d) confirms a realistic realization of the in situ observations by the model. The differences in the stratification should have a negligible impact when comparing vertically integrated energy fluxes from STORMTIDE2 with mooring results.

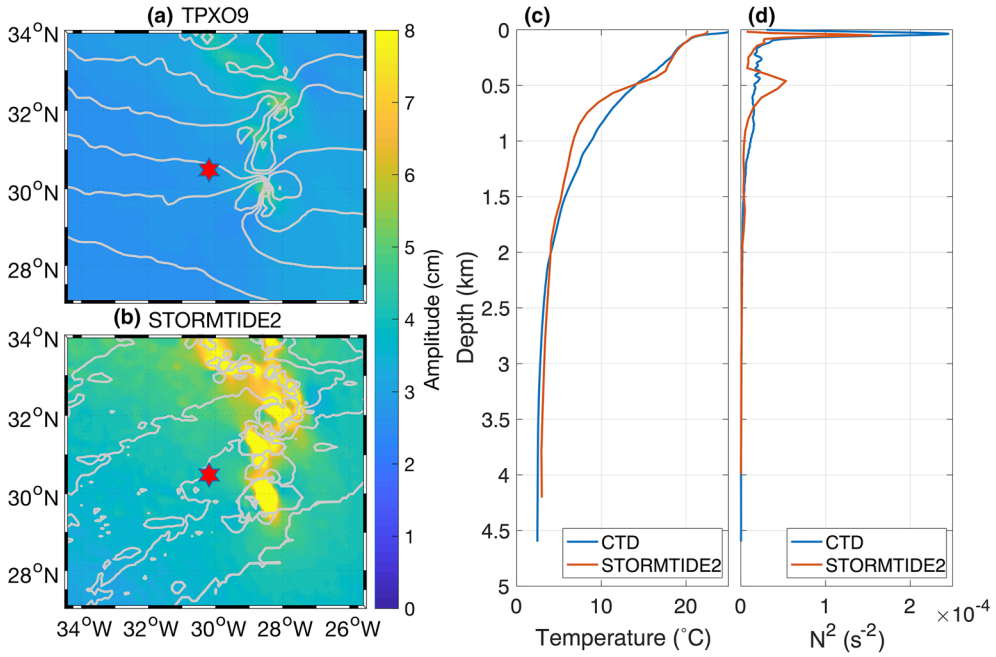

Figure 2. Co-tidal charts of (a) TPXO9 and (b) STORMTIDE2, and mean profiles of (c) temperature T and (d) stratification (buoyancy frequency N^2). Gray contour lines in (a) and (b) represent the phase of the amplitude in 5° steps; red stars indicate the position of the mooring.

2.3. Other Datasets

Global maps of internal wave energy fluxes in the semidiurnal M_2 band for the first and second mode were obtained from satellite altimetry (Zhao, 2018; Zhao et al., 2016). The sea surface height (SSH) expressions of modes 1 and 2 of the internal tide were obtained from multiple satellite altimeters during 1992–2012, representing a 20-year mean. A two-dimensional plane wave fit method, with fitting windows of 160 × 160 km for mode 1 and 120 × 120 for mode 2, was used to extract the coherent energy flux from altimetric SSH data.

For the calculation of surface eddy kinetic energy (EKE) a satellite-based altimetry dataset provided by E.U. Copernicus Marine Service Information (CMEMS) has been used (SEALEVEL_GLO_PHY_L4_REP_OBSERVATIONS_008_047). The dataset contains multimission altimeter satellite gridded SSHs and derived variables computed with respect to a 20-year mean. All satellite missions are homogenized with respect to the reference Ocean Surface Topography Mission/Jason-2. The data processing removes any residual orbit error, long wavelength error, and large biases and discrepancies between various data flows. After a cross

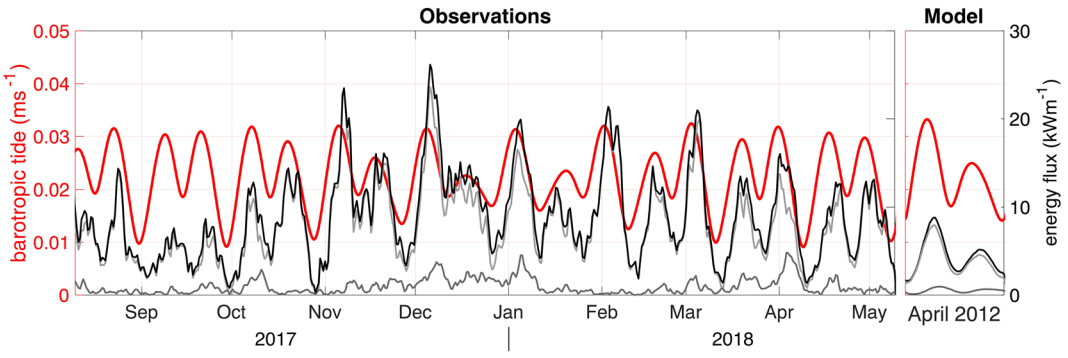

Figure 4. Black: Sum of mode 1 and mode 2 of semidiurnal energy flux from the mooring observations, example month from STORMTIDE2 model as a representation of the model time series shown as comparison. Light gray and dark gray are the first and second mode of the semidiurnal energy fluxes respectively; red: amplitude of the barotropic tide as the sum of the first 4 (M_2, S_2, N_2, and K_2) tidal constituents from TPXO9 at the mooring location.

validation, the sea level anomaly (SLA) is subsampled. Geostrophic currents are then derived from the SLA data.

2.4. Method

The calculations of internal wave energy fluxes are adapted from Alford and Zhao (2007) and Nash et al. (2005), and are laid out briefly in the following. These calculations are the same for the mooring and the STORMTIDE2 model. For the model each vertical layer is treated as if it would be a single point instrument in a mooring, and the internal tide induced vertical displacement is calculated using the temperature gradient via the relation

$$\eta(z_i,t) = T(z_i,t) / T_z(z_i),$$

where the vertical temperature gradient $T_z(z_i)$ is computed from the mean of the entire time series. $T(z_i,t)$ is the band pass filtered temperature measured at depth z_i and time t. The stratification of the mooring time series in the lower part of the water column is too weak to calculate a vertical displacement from the temperature measurements, as its gradient $T(z)$ falls below the threshold of 3×10^{-5} m^{-1} as given in Alford and Zhao (2007). Thus, the displacements from the deepest two sensors for this calculation should be removed. To avoid this, the vertical displacement for all depths of the mooring time series is directly calculated from the M_2 filtered vertical velocities. To use the velocity data of the Quartermaster ADCP, its vertical component had to be filtered for diurnal plankton migration. This filter was adopted from Fischer and Visbeck (1993).

Over flat bottom, the vertical structure of internal waves can be represented by a superposition of discrete vertical modes which depend only on the buoyancy frequency $N(z)$ and which are defined as solutions of the eigenvalue problem

$$\frac{\partial^2}{\partial z^2}\eta(z) + \frac{N^2(z)}{c_n^2}\eta(z) = 0$$

with the boundary conditions $\eta(0) = \eta(H) = 0$, mode number n, water depth H, eigenspeed c_n, buoyancy frequency $N(z)$ and the vertical displacement $\eta(z)$ at depth z. The structure of mode 1 and mode 2 was calculated using iModes, a MATLAB toolbox for the modal solutions of the internal wavefield (Haji, 2015; Saidi, 2011); profiles of filtered horizontal velocities and vertical displacements were projected onto a linear combination of these modes, thus obtaining a full depth-profile. The depth integrated horizontal energy flux for each mode can then be obtained from the covariance of the modal velocity $u(z')$ and baroclinic pressure anomaly $p'(z')$ with

$$F = \int_{-H}^{0} \langle u(z')\, p'(z') \rangle dz',$$

where $\langle\ \rangle$ is the average over one wave period. For each mode the baroclinic pressure anomaly $p'(z)$ is calculated via the vertical displacement, the buoyancy frequency $N(z)$, and the vertically averaged density $\overline{\rho}$ (Kunze et al., 2002):

$$P_n'(z) = \int_{-z}^{0} N^2(z') \cdot {}_n(z')dz' - \overline{p_n} \text{ with } \overline{p_n} = \int_{-H}^{0} N^2(z') \cdot {}_n(z')dz'.$$

Based on the number and the vertical distribution of instruments and following the estimates given in Nash et al. (2005), we consider the systematic error to be <5% for the energy fluxes from the mooring data and <l% for the STORMTIDE2 data. For the measured and modeled time series, given confidence intervals of the mean values are calculated as 95% bootstrapped confidence intervals with 10^4 repetitions. A close up of the sum of mode 1 and mode 2 meridional velocity, vertical displacement, and pressure anomaly, as well as the resulting vertically depth integrated energy fluxes, are shown in Figure 3 for the mooring time series. The modal solutions of horizontal velocities and vertical displacement are in general representative for the discrete filtered data. The velocity data, of which the barotropic component was removed, are surface

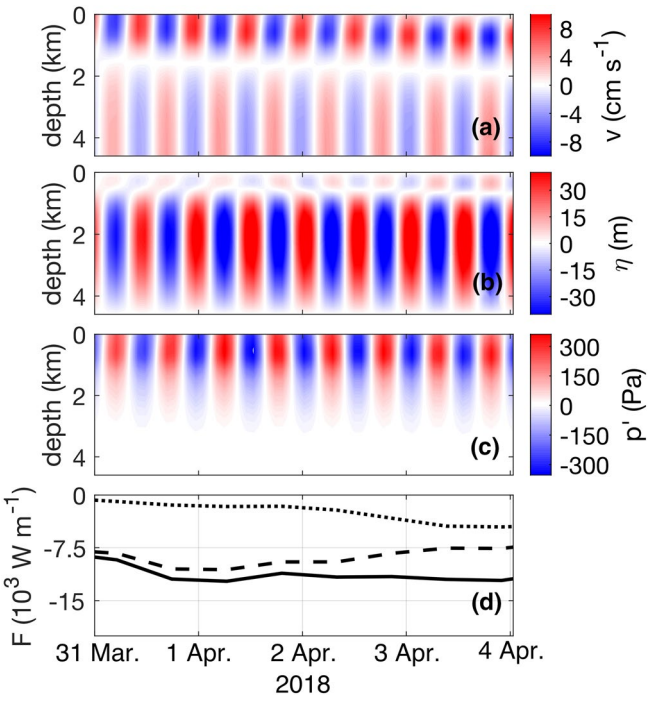

Figure 3. Details of the energy flux calculations from mooring time series; (a) sum of the mode 1 and mode 2 meridional velocity for the first peak in the spring-neap cycle during April; (b) sum of mode 1 and mode 2 vertical displacements; (c) sum of mode 1 and mode 2 pressure anomaly; (d) depth integrated meridional energy flux mode 1 (dashed line) mode 2 (dotted line) and their sum (solid line).

intensified owing to the weaker stratification at the bottom. Large shallow values of the vertical displacement cannot be represented by a sum of mode 1 and mode 2, and are therefore absent. The baroclinic pressure anomaly reveals values of about 350 Pa, which results in surface elevations of about 3.5 cm, which agrees with data from satellite altimetry. The resultant energy flux is the covariance of velocity and pressure anomaly and is therefore strongly surface intensified (not shown, Alford and Zhao [2007]).

Following Zhao et al. (2010), the band passed semidiurnal internal tide is decomposed into a coherent and an incoherent component for each mode. M_2 and S_2 signals are harmonically fitted using the T_TIDE analysis software (Pawlowicz et al., 2002). For each component (M_2 and S_2) the energy flux is calculated following the procedure described above and the total energy flux of the semidiurnal internal tide is defined as

$$F_{\text{semi}} = F_{M_2} + F_{S_2} + F_{\text{in}},$$

where F_{semi} is the energy flux for the band pass filtered semidiurnal component, F_{M_2} and F_{S_2} are the harmonically fitted coherent parts of the energy flux for M_2 and S_2 respectively, and F_{in} the incoherent part of the energy flux.

To infer a potential influence of changes induced by the background flow field on the internal tide energy flux, we calculated EKE from 40 h low-pass filtered horizontal velocities (u,v) of all current meter time series at all instrument depths. A corresponding time series of surface EKE was calculated using the CMEMS data set. The EKE is defined as:

$$\text{EKE} = \frac{u^2 + v^2}{2}$$

To further investigate the influence of the background flow field, spectra of vertical (w) and horizontal (u, v) baroclinic velocities of the measured time series were calculated by projecting them onto the corresponding mode structure with a least square fit. From the resulting full depth modal velocities, the power spectral density was estimated for each mode using half-overlapping 1-week windows.

3. Energy Flux From In Situ Observations

We focus on the analysis and description of the temporal variability of the energy flux associated with the semidiurnal internal tide and its causes. For this analysis, we look at the magnitude and direction of the energy flux, changes in the coherent part of the energy flux and the modal composition. Figure 4 shows the development of the energy flux in the first two modes during the mooring deployment as well as the barotropic tide from TPXO9 at the mooring location. The semidiurnal energy fluxes show a strong spring-neap variability, especially in the first mode but to a lesser degree also in the second mode. The amplitude of the total energy flux is clearly dominated by mode 1 which is often indistinguishable from the total energy flux. On average, the fraction of the first mode in the total energy flux is 88% ± 1% (Figure 5, lower panel). The mean of the semidiurnal energy (first mode plus second mode) in the mooring observation is 9.02 ± 0.42 kW m^{-1} (Table 2), with peaks up to 26.17 kW m^{-1}. We calculated that 92% of the sum of the energy flux in modes 1 and 2 of the mooring time series is coherent, leaving the rest in the incoherent part. In mode 2 only 64% of the energy flux is coherent. The fraction of the first mode changes to 92.6% ± 0.01% by looking only at the coherent part of the energy flux.

The steadiness of the energy flux at the mooring location is demonstrated by the time series of its direction. The mean direction of the semidiurnal mode 1 energy flux is 224° ± 3° and does not vary much in time, whereas the mean direction of mode 2 energy flux is at 204° ± 4° (Figure 5). The peaks in the measured

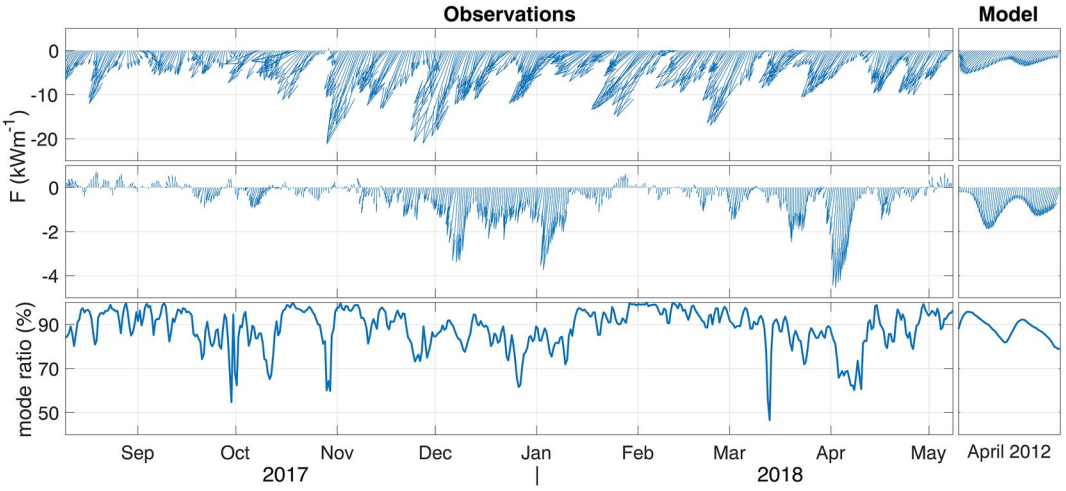

Figure 5. Directional variability and magnitude of energy flux for mode 1 (upper panel) and mode 2 (middle panel) from the mooring time series; example month from STORMTIDE2 model as a representation of the model time series shown as comparison. Note the different scaling of the *y*-axis for mode 1 and mode 2; lower panel: ratio between first and second mode of energy fluxes; 80% means that the combined mode 1 and mode 2 flux consists of 80% mode 1 and 20% mode 2 at the corresponding time.

energy flux lag those of the barotropic tide from TPXO9 (Figure 4). This time lag can be used for a rough estimate of the possible generation site using the group speed of mode 1 and mode 2 waves to infer the covered distance. This was done for five representative peaks for mode 1 and three representative peaks for mode 2. The distance for mode 1 ranges from 124 km up to 451 km with a mean of 266 km. The estimated distance for mode 2 ranges from 128 km up to 235 km with a mean of 185 km. These distances in combination with the mean direction of the energy flux point toward the seamount chain south of the Azores as generation site for the observed internal tides, confirming the earlier study by Köhler et al. (2019).

The background internal wavefield can be distorted by interactions with mesoscale flow, for example by inducing changes in internal wave propagation directions. To quantify these distortions, we calculated a distortion metric (d) following Dunphy et al. (2017), who analyzed the propagation of internal tides through a turbulent eddy field in numerical experiments. d is defined as the standard deviation of the energy flux normalized by the mean of the energy flux (Table 2, square brackets). For the semidiurnal components this

Table 2
Mean Energy Flux for the Mooring, the STORMTIDE2 Model, and Satellite Altimetry in the Semidiurnal Band, M_2+S_2 Coherent and M_2 Coherent Part

	Semidiurnal flux (kW m^{-1})			M_2+S_2 coherent flux (kW m^{-1})			M_2 coherent flux (kW m^{-1})		
	Mode 1	Mode 2	Total	Mode 1	Mode 2	Total	Mode 1	Mode 2	Total
Mooring total	8.04 ± 0.39 [0.05]	0.96 ± 0.08 [0.08]	**9.02** ± 0.42 **[0.05]**	7.68 ± 0.03	0.61 ± 0.01	**8.29** ± 0.03	7.02 ± 0.01	0.46 ± 0.01	**7.48** ± 0.01
Mooring no eddy	9.55 ± 0.76 [0.08]	1.53 ± 0.16 [0.10]	**11.07** ± 0.86 **[0.08]**	9.21 ± 0.02	1.34 ± 0.00	**10.55** ± 0.02	8.67 ± 0.02	1.24 ± 0.00	**9.91** ± 0.02
Mooring surface eddy	6.57 ± 0.70 [0.11]	0.60 ± 0.08 [0.13]	**7.16** ± 0.73 **[0.10]**	5.83 ± 0.03	0.28 ± 0.00	**6.10** ± 0.03	5.17 ± 0.01	0.21 ± 0.00	**5.39** ± 0.01
Mooring subsurface eddy	8.80 ± 0.99 [0.11]	0.75 ± 0.12 [0.16]	**9.55** ± 1.01 **[0.11]**	8.21 ± 0.03	0.39 ± 0.00	**8.60** ± 0.03	7.36 ± 0.02	0.35 ± 0.00	**7.71** ± 0.02
STORMTIDE2	3.97 ± 0.23 [0.06]	0.41 ± 0.03 [0.07]	**4.39** ± 0.24 **[0.05]**	3.76 ± 0.05	0.40 ± 0.01	**4.16** ± 0.05	3.51 ± 0.04	0.36 ± 0.01	**3.87** ± 0.04
Satellite altimetry	/	/	/	/	/	/	1.76	0.08	**1.84**

Note. Distortion parameter d is given in square brackets for the semidiurnal energy flux.

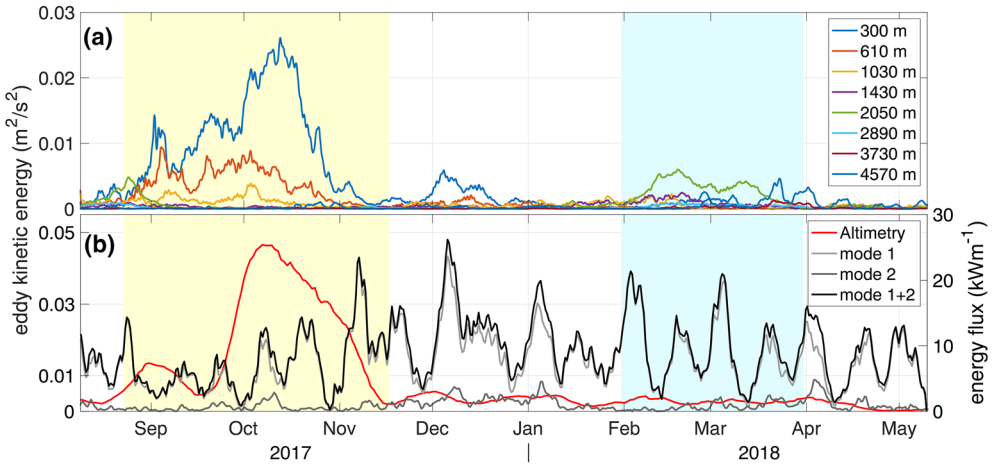

Figure 6. Eddy kinetic energy (EKE) at the mooring location from the moored current meters and from CMEMS (red line in b). Also shown in (b) is the observed energy flux of the semidiurnal internal tide. Different background colors indicate eddy activity: yellow = surface eddy; blue = subsurface eddy; white = no eddy.

yields 0.05 for mode 1 + 2 (0.05 mode 1 and 0.08 mode 2). The change of the distortion parameter by interactions of the wavefield with eddies is further examined in Section 4.

The dominance of mode 1 is consistent with findings by Vic et al. (2018) and open-ocean mooring estimates of energy flux from the internal waves across the Pacific experiment (Zhao et al., 2010). In contrast to Vic et al. (2018), we do not find a high directional variability of internal tides which they linked to multiple sources around their mooring. This is likely due to the position of the mooring, where the interference patterns of different wave trains from different sources form a beamlike structure with a distinct direction (Köhler et al., 2019). The directional variability on short time scales might be attributed to reflection, scattering, and interferences between waves from different sources (Zaron & Egbert, 2014).

A poorer correlation with the barotropic tide and higher variability in the direction of mode 2 energy flux compared to mode 1 is consistent with findings by Ansong et al. (2017), where historical mooring observations on a global scale were compared with a high resolution numerical model (HYCOM). They also found almost constantly lower magnitudes of energy flux of mode 2 compared to mode 1. A larger incoherent proportion in the second mode in comparison to the first mode might be expected due the more complex structure of the second mode which makes it more susceptible to disturbances (Ponte & Klein, 2015).

Beside the strong spring-neap variability, we found a strong temporal variability on subseasonal time scales, that we attribute to interaction with the mesoscale flow. The presence of eddies and their influence on the energy flux is evaluated in Section 4. We did not see any other temporal variability for example in terms of seasonal changes in the energy flux for M_2, which reinforces the assumption that the temporal variability of internal tides is primarily due to the presence of mesoscale eddies, with the constant forcing of the tides (Ponte & Klein, 2015; Zaron & Egbert, 2014). Also, Shriver et al. (2014) found that the energy flux in the vicinity of strong generation regions, like the seamount chain south of the Azores, tends to be less variable than in regions of weak forcing.

4. Eddy—Internal Tide Interaction

At the beginning of the time series, between August and November, the observed energy flux of the internal tide is notably lower compared to the remaining months of December to May. We formulated the hypothesis that this decrease of the energy flux is caused by interaction with mesoscale features. To test this, we calculated EKE from the current meter time series, and also EKE from the CMEMS satellite altimetry dataset (Figure 6). The EKE measured by the current meters shows higher values between the end of September and mid of October as well as between February and April. During the first period the EKE from CMEMS confirmed the presence of a surface intensified mesoscale eddy. In addition, the EKE from the mooring

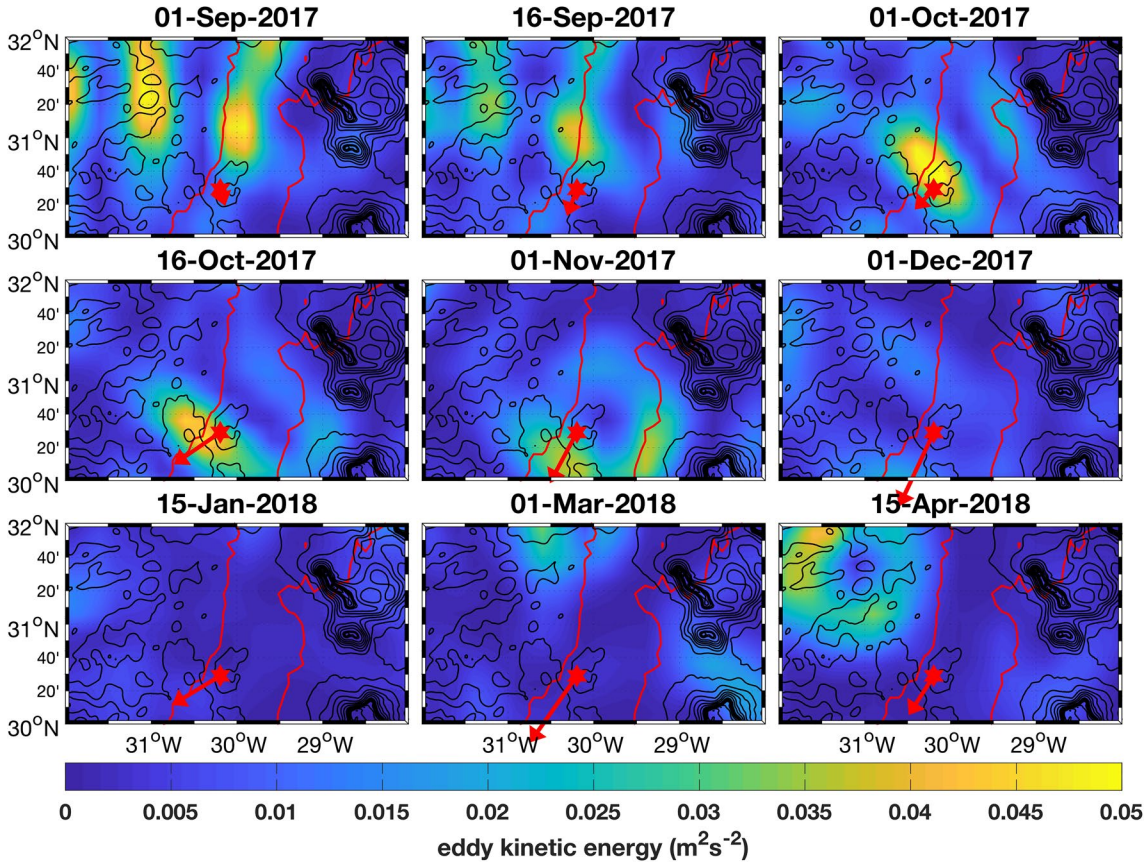

Figure 7. Eddy kinetic energy (EKE) at selected times during the mooring deployment calculated from satellite altimetry. Red star and arrow: Mooring location and the total semidiurnal energy flux as the mean of the given day ±10 M_2 periods (~5 days). Red contour line: 1.8 kW m^{-1} contour line of mode 1 and mode 2 energy flux from satellite altimetry (as shown in Figure 1a) as an indicator for the tidal beam. Black contour lines of bathymetry for every 100 m in the upper 1,000 m and every 500 m for the rest of the water depth.

indicated the presence of a subsurface eddy in the second period. This subsurface eddy was not visible in the EKE from CMEMS. We then split the measured energy flux time series of the mooring in a surface eddy, a subsurface eddy, and a no-eddy time period which is in between the two eddy periods, to further investigate the influence of these eddies on the variability of the energy flux time series.

During the remaining time of the observations there was no further surface eddy present in the altimeter data, neither at the mooring location, nor inside the tidal beam between mooring location and generation site. This is important because interactions between internal tides and mesoscale motions would also happen at these "upstream" locations which would lead to biased measurements at the mooring. We cannot exclude further subsurface eddies outside the mooring location, as they are not detectable by satellites. The development of the surface eddy is shown in Figure 7.

During the periods when the eddies were present at the mooring location, the characteristics of the internal tide beam changed considerably, indicating an interaction between the mesoscale structures and the internal tide. The energy fluxes in the first and second mode during the surface eddy period are about 35% lower (−31% for mode 1, −61% for mode 2) than during the time period when no eddy is present (Table 2). The subsurface eddy seems to affect mainly the second mode, leaving the first mode almost intact. Here the calculated energy fluxes in the first and second mode for the semidiurnal band are about 14% lower (−8% for mode 1, −51% for mode 2) than during the time period when no eddy is present, with the second mode intermittently reaching almost zero. The mean energy flux for the sum of the first and second mode in the no-eddy period is 11.07 ± 0.86 kW m^{-1}. The distortion parameter d is 0.08, for the sum of mode 1 and mode 2 (0.08 and 0.10 for modes 1 and 2, respectively) during the no-eddy period. It increases during the surface eddy period to 0.10 (0.11 for mode 1, 0.13 for mode 2) and during the subsurface eddy period to 0.11 (0.11

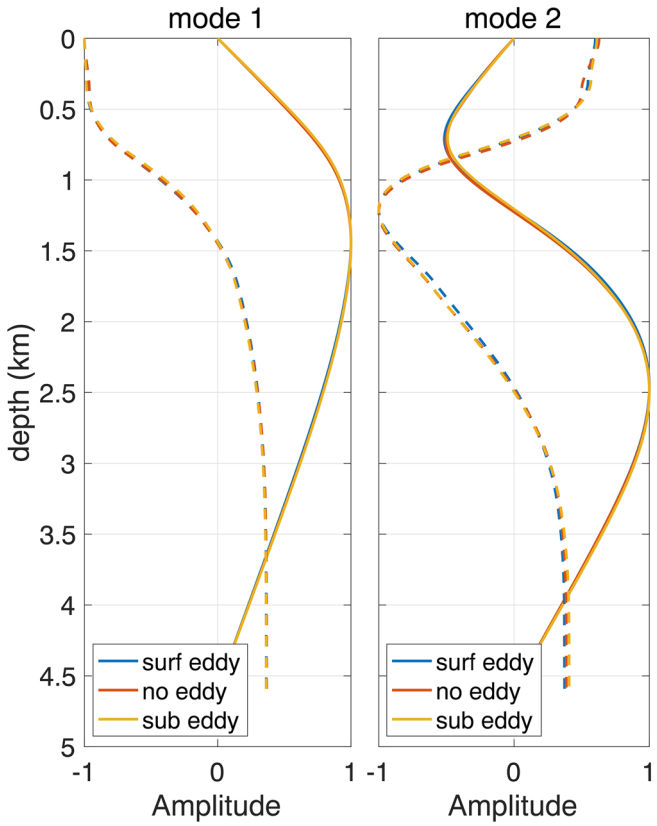

Figure 8. Structure of the first two vertical baroclinic modes for vertical displacement (solid line) and horizontal velocities (dashed line) during surface eddy (blue), no-eddy (red), and subsurface eddy (yellow) periods show a negligible impact of the eddy induced changes in stratification on the mode structure.

for mode 1, 0.16 for mode 2). For comparison, in Dunphy et al. (2017) the distortion metric increases from 0.08 to 0.21 in the zonal component and from 0.04 to 0.50 in the meridional component for mode 1 of the energy flux by interaction with a quasigeostrophic turbulent field in numerical experiments.

In situ measurements of the decay of the internal tide energy away from the generation site help to estimate the amount of energy that is available for mixing. However, due to interference of waves from multiple generation sites (Rainville et al., 2010; Zaron & Egbert, 2014) and constructive and destructive interference from interaction with mesoscale eddies (Dunphy & Lamb, 2014), the correct interpretation of in situ measurements is complicated. The decrease of the energy flux in the low modes during the eddy periods can be explained by their interaction with mesoscale motions (Dunphy & Lamb, 2014; Dunphy et al., 2017; Kelly & Lermusiaux, 2016; Kelly et al., 2016; Kerry et al., 2014; St. Laurent & Garrett, 2002; Rainville & Pinkel, 2006) which affects the propagation of all modes, although the effect increases with increasing mode number. These interactions can modify the propagation path, group and phase speed, lead to wave reflection and/or transfer energy from lower to higher modes which is conducive for increased wave breaking and in turn may lead to stronger local mixing. Kerry et al. (2014) found that the mesoscale circulation enhances the internal tide dissipation by a factor of 2–5 when subtidal circulation is considered, compared to a horizontally uniform stratification. They relate this enhanced dissipation to interaction with sheared currents in the upper ocean which may cause scattering of low-mode internal tides to higher modes, which have a greater downward propagation of energy and may therefore contribute to deep-ocean mixing (Whalen et al., 2018). The different response of mode 1 and mode 2 to the presence of eddies may be attributed to the different susceptibility of the modes to interact with the modal structure of the eddies. Because of its more complex vertical structure, the second mode is more susceptible for disturbances, especially in a depth of about 2,000 m where the gradient of horizontal velocity is higher than in the first mode, and where the maximum of the subsurface eddy is located (Figure 8). A stronger influence onto the second mode was also found by Dunphy et al. (2017) who used the distortion metric in numerical experiments to confirm that the variability increases when a low-mode internal tide propagates through a quasigeostrophic turbulent field. With our in situ observations, we can confirm an increase in the distortion metric during eddy time periods, and that mode 2 waves are indeed distorted more strongly than mode 1 waves.

Comparing the ratio of coherence between the eddy and no-eddy phases of the time series, it is observed that the ratio between the coherent and incoherent part of the energy flux goes from 95% (96% mode 1, 88% mode 2) during the no-eddy period down to 85% (89% mode 1, 47% mode 2) during the surface eddy period and to 90% (93% mode 1, 52% mode 2) during the subsurface eddy period. Focusing on the M_2 coherent part, the energy flux is 46% lower for the sum of modes 1 and 2 (−40% for mode 1 and −83% for mode 2) during the surface eddy period compared to the no-eddy period in the time series and 22% lower for mode 1 + 2 (−15% for mode 1, −72% for mode 2) during the subsurface eddy period. The decrease of coherence and simultaneous increase of incoherence during eddy periods in comparison to the no-eddy period is particularly pronounced in the second mode but can also be identified in the first mode.

Our observations support the results from studies based on numerical models and on a combination of model and altimetry (e.g., Ponte & Klein, 2015; Rainville & Pinkel, 2006) that showed that eddy interaction increases incoherence and that this effect becomes more important with increasing mode number. Stronger incoherence of the internal tides affect their predictability and may influence the ability to estimate the ocean circulation from high resolution altimetry (Richman et al., 2012). The higher incoherence of the

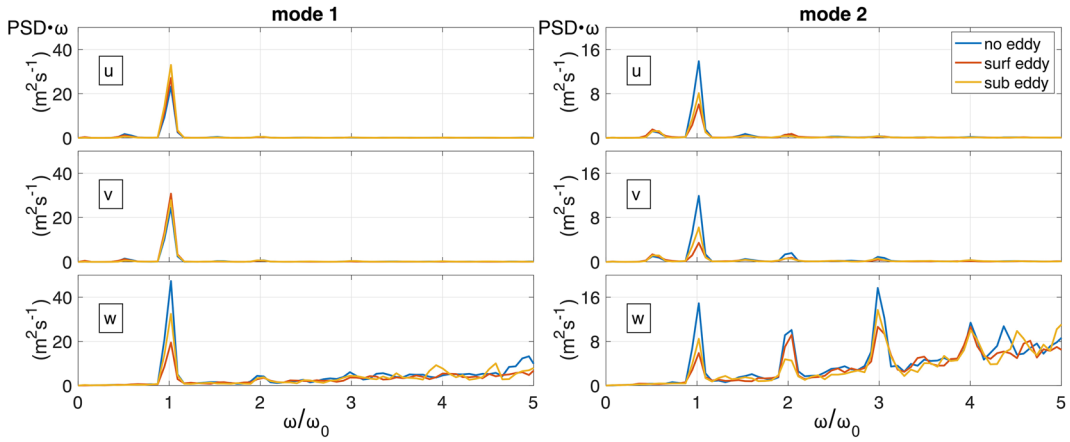

Figure 9. Power spectral density (PSD) of mooring observations after projection of horizontal (u,v) and vertical (w) velocities onto mode 1 and mode 2 shows differences between no-eddy (blue), surface eddy (red), and subsurface eddy (yellow) phase. The influence of the eddies is most prominent for the vertical velocity but also occur in mode 2 in all velocity components. x-axis is scaled by forcing frequency $\omega_0 = M_2$ and y-axis multiplied with frequencies ω.

second mode during the subsurface eddy period in comparison to the surface eddy period can again be attributed to the vertical mode structure of horizontal velocity and its stronger gradient at a depth of 2,000 m where the subsurface eddy is strongest.

Another aspect is the change in stratification caused by the presence of eddies, and whether these changes in the stratification have a considerable impact on the resulting mode shapes. To answer this, we assumed that the main density changes in the stratification profile are caused by temperature, leaving salinity constant over time. We took the salinity values from the repeated CTD casts close to the mooring location, which we used for the stratification in the first place, and calculated "pseudo" stratification profiles for each time step with the temperature from our mooring. We then calculated mean stratification profiles for the surface eddy, no-eddy, and subsurface eddy time period and computed the corresponding mode structure. The resulting differences in the mode structure are marginal (Figure 8). Therefore, we can exclude that the use of a temporally constant stratification significantly affects our energy flux calculation. Note that this is in contrast to the results of Zaron and Egbert (2014) who found that refraction, caused by changes of the background stratification, is one of the main drivers for the variability of the internal tide response at the Hawaiian Ridge. It is likely that the changes in stratification in our research region are too small to yield this effect. In general, reflection and scattering of internal waves occur when they propagate across horizontally varying topography or stratification. In our case, the horizontal buoyancy gradients are relatively weak, therefore topographic effects should dominate (Q. Li et al., 2019).

To further investigate the influence of mesoscale eddies on the energy flux variability, we calculated the power spectra of the amplitude of detrended baroclinic modal vertical and horizontal velocities (Figure 9). These spectra show higher peaks during no-eddy periods than during eddy periods, supporting the conclusion above that eddy interaction is damping the energy flux in the first and second mode. It might be an indication of a scattering of energy toward higher modes (not resolved by the mooring), which could ultimately lead to an increased local dissipation. Interestingly, this relation is not observed in the first mode of the horizontal velocity component. Here are several plausible hypotheses:

1. Rainville and Pinkel (2006) observed that mesoscale variability can lead to refraction of the propagation path of internal tides. This leads to a shift of the propagation path of the individual modes, whereby the effect increases with mode numbers. This reduces coherence and, as we noticed in our observations, increases incoherence of the energy flux during eddy periods, especially in the second mode. Apart from that, we do not see a reasonable change in the stratification during the eddy periods which is another indicator for the refraction of internal tides (Zaron & Egbert, 2014).
2. Given that the pattern of internal waves emanating from different topographic generation sites is non-uniform, the eddies could shift the interference pattern of single waves from different sources (Dunphy

& Lamb, 2014; Kelly & Lermusiaux, 2016; Rainville et al., 2010), and might shift even the interference pattern of the different modes individually. An indication toward this explanation might be a stronger directional variability during the eddy periods.

3. The eddies could, because of their mostly horizontal mode 1 structure, pump energy into the first horizontal mode which is then directly scattered away into higher modes. This theory might explain why we do not see differences in the individual eddy phases in the horizontal component of mode 1, but it remains questionable why the eddies would pump energy specifically into the M_2 frequency.

The differences in the first mode between vertical and horizontal velocity components could explain why the second mode of the energy flux is more strongly affected by the eddies. The reduction of energy flux via eddy interaction would rely in the first mode only on the vertical (displacement), while in the second mode also the horizontal velocities are affected. It remains unclear which process is the main driver for the different behavior of the horizontal component in the first mode or in which way the individual effects act on the observed internal tides as a whole.

Interesting to note is a variety of smaller peaks at each harmonic of the M_2 frequency, strongly emphasized at the vertical component (w) of mode 2 (Figure 9). They result from the scattering of energy to higher frequencies, and are assumed to be a result of various wave-wave interactions (Dunphy & Lamb, 2014; Dunphy et al., 2017). One can argue that by band-pass filtering only around the generation frequency M_2, some of the energy in the semidiurnal band will not be considered in the calculation of the energy flux of the internal tide as it is transferred to higher harmonics. Especially in the second mode, the second and third harmonics of M_2 seem to have a similar amount of energy as the generation frequency.

5. Comparison With Model and Altimetry

To quantify the capability of an OGCM to represent in situ observations, we compare several quantities (mean energy flux, modal composition, coherence, and direction of energy flux) derived from our mooring data with the energy flux calculated from the STORMTIDE2 model output, and that derived from satellite altimetry. This comparison is motivated by the question of how good an OGCM such as STORMTIDE2 that is not specifically tuned to mimic our measurements is representing the characteristics of the energy flux in strong generation regions of internal tides. We focus on the energy flux of the internal tides in general, since this quantity is relatively easy to examine for this kind of models. Moreover, it is an important benchmark since its divergence identifies sources and sinks of energy. Usually, a point-wise comparison of measurements with a model or other large dataset can be problematic for various reasons, for example because of spatial and temporal averaging or interference patterns of multiple waves. Figure 10 shows the location of our mooring in the context of the energy flux calculated from the STORMTIDE2 model output. The semidiurnal energy flux from STORMTIDE2 is varying in direction and magnitude in the wide region around the mooring location, with a distinct tidal beam in southwest direction. Closer to the mooring location in the tidal beam, however, the model shows a more homogenous picture (Figure 10, inset). Therefore, we compare the closest grid point of STORMTIDE2 with the energy flux derived from satellite altimetry, and from our mooring data.

The energy fluxes from STORMTIDE2, as well as the mooring data, show a strong spring-neap variability clearly dominated by mode 1 (Figure 4). The time mean for the STORMTIDE2 semidiurnal energy flux for the sum of the first and second mode is 4.39 ± 0.24 kW m^{-1} (Table 2), with peaks up to 9.34 kW m^{-1}. This corresponds to an underestimate of the energy flux by the model of a factor of about 2 in comparison to the mean of the mooring time series.

From the satellite altimetry it is only possible to extract the coherent part of the energy flux (Zhao et al., 2016), so the results from the altimetry can only be compared to the M_2 coherent portion of the in situ measurements and of STORMTIDE2. Energy fluxes calculated from satellite altimetry show 1.84 kW m^{-1} as the sum for the first and second mode. In comparison, the M_2 coherent part of the energy flux from in situ measurements (7.48 ± 0.01 kW m^{-1}) and from STORMTIDE2 (3.87 ± 0.04 kW m^{-1}) is higher by factors of about 5 and 2, respectively. In the M_2 coherent part, the underestimate of STORMTIDE2 compared to the mooring time series is also a factor of about 2.

Ninety-five percent of the sum of the energy flux in mode 1 and mode 2 (95% mode 1, 98% mode 2) in the STORMTIDE2 model is coherent (Table 2). Hence, model and observations agree on the amount of

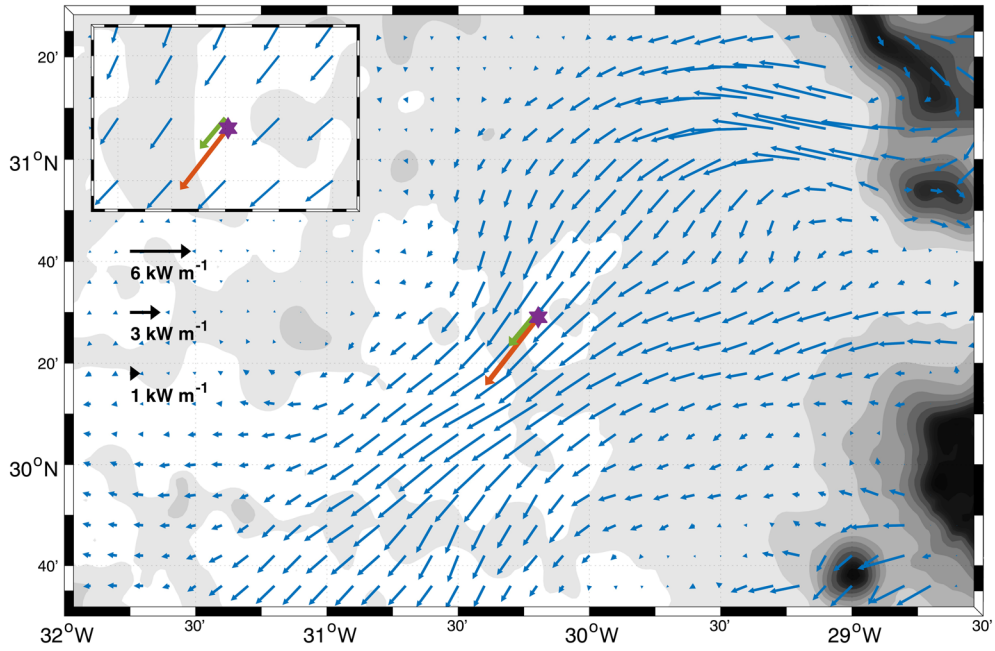

Figure 10. Position of the mooring in relation to the net energy flux calculated from STORMTIDE2. Purple star: mooring location; red arrow: net semidiurnal energy flux from mooring time series; green arrow: net semidiurnal energy flux from STORMTIDE2 at the grid point closest to the mooring location; blue arrows: net semidiurnal energy flux from STORMTIDE2; reference arrows for the main map at the left side. Inset upper left corner shows a zoom focused on the mooring position. Background: gray shading of bathymetry for every 100 m in the upper 1,000 m and every 500 m for the remainder of the water depth.

incoherent energy flux for the first mode but differ on how much energy is in the incoherent part of the second mode. The fraction of the first mode in the total energy flux in STORMTIDE2 is 90% ± 1%, for the M_2 coherent part of the energy flux the ratio changes to 90.7% ± 0.3%. For the energy flux derived from satellite altimetry, the fraction of the first mode is 93% ± 1%. Hence, all three datasets agree that the total energy flux contains between 7% and 12% mode 2 in the M_2 coherent part.

The direction of the STORMTIDE2 energy flux does not vary much in time. This is true not only for the first, but also for the second mode. The mean direction of the M_2 semidiurnal component in STORMTIDE2 is 230° ± 1° for mode 1 and 224° ± 7° for mode 2. This puts the mean direction of mode 1 of the energy flux in the semidiurnal component from observations in a good agreement with the mode 1 mean directions from STORMTIDE2, and to a lesser degree also in mode 2 (Figure 11). Comparing the M_2 coherent part of the energy flux from the mooring with the M_2 coherent part of STORMTIDE2 results in an even better agreement in the first mode. In this case the mean direction of the first mode in STORMTIDE2 is 230° ± 0.5°. The mean direction in mode 2 of the M_2 coherent energy flux in STORMTIDE2 is 243° ± 4°. For comparison, the direction of the energy flux derived from satellite altimetry is 244° for mode 1 and 274° for mode 2. In general, we see a better agreement between the three datasets in the first mode than in the second.

The significantly weaker energy flux in the STORMTIDE2 model (in the total semidiurnal band, as well as in the M_2 coherent case) in comparison to the energy flux from the measurements is most likely caused by an unrealistically high (numerical) damping in the model (Köhler et al., 2019; Müller et al., 2012). Another possible explanation for the lower energy flux in STORMTIDE2 could be an insufficient barotropic to baroclinic energy conversion rate at the seamount chain where the observed internal tides are generated. But this aspect is likely less prevalent considering that STORMTIDE2 does not underestimate the barotropic velocities, as discussed in Section 2. The underestimate of the M_2 coherent energy flux by the satellite altimetry in comparison to the measurements and STORMTIDE2 likely results from the large spatial and temporal averaging of the satellite data. For the calculation of the energy flux from satellite altimetry, data from more than 20 years of observations have been used. The fitting window is large in comparison with the total

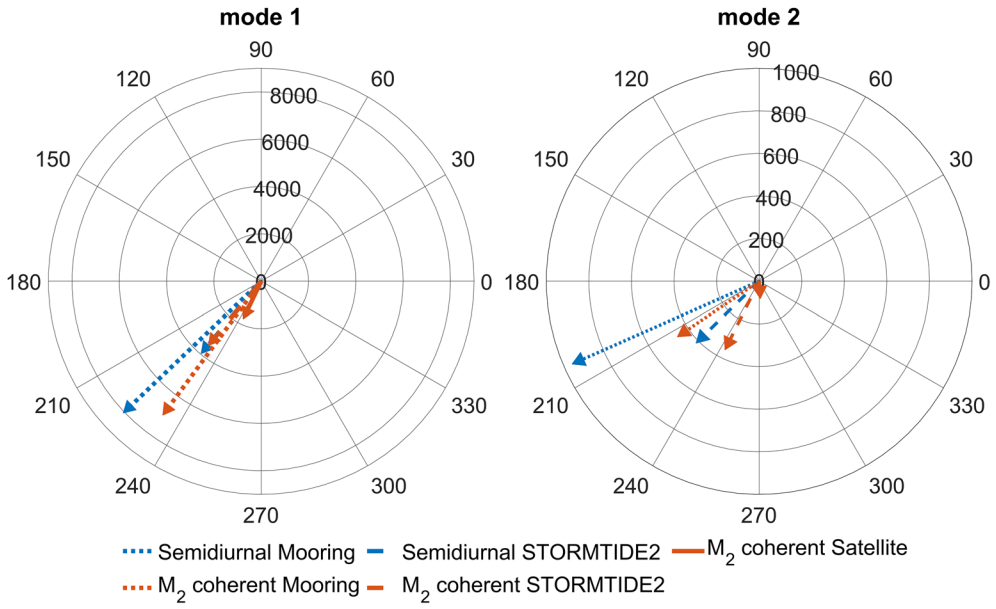

Figure 11. Mean amplitude and direction of the total semidiurnal energy flux (blue) and the M_2 coherent energy flux (red) of the mooring time series (short dashed), STORMTIDE2 (dashed) and satellite altimetry (continuous) for the first and second mode.

width of the tidal beam which is about 150 km (Zhao, 2018; Zhao et al., 2016). Because of this discrepancy we expect a smeared amplitude of energy flux in this dataset.

The higher coherence in the model compared to the in situ measurements possibly results from a weaker background variability, which leads to fewer interactions with mesoscale motions. Because of its resolution, STORMTIDE2 is also not able to resolve wave-wave interactions, representing another missing aspect that leads to an increase in incoherent energy flux.

The STORMTIDE2 model shows a weak mesoscale variability in comparison to the measurements in the region south of the Azores. We calculated the EKE in the available model output, but could not identify a clear eddy signal. Hence, we are not able to compare the observed eddy—internal tide interactions with a similar situation in the model. While a direct comparison of our in situ observations with the STORMTIDE2 model is not possible, we compared the no-eddy period of the observations with the "background" state in the model. However, the comparison between the in situ observations and STORMTIDE2 is not improved by this restriction. Comparing the semidiurnal energy flux during the no-eddy period with STORMTIDE2 increases the underestimate to a factor of 2.5. Comparing only the M_2 coherent part during the no-eddy period of the mooring with the STORMTIDE2 average results in an underestimate of a factor of 2.3 and in a factor of 5.4 for energy fluxes derived from satellite altimetry. Comparing the M_2 coherent energy flux during the surface eddy period with the energy flux from satellite altimetry results in a factor of 2.9. This might be a more reasonable comparison with the energy flux dataset derived from satellite altimetry due to the loss of coherence associated with eddy interaction, with the altimetry only being able to detect the coherent part of energy.

6. Summary and Conclusions

We analyzed the low-mode internal tide energy fluxes and their temporal variability in an internal tide beam south of the Azores. We investigated the amount of coherent energy flux, the direction of the energy flux and its modal composition, as well as the influence of a surface and a subsurface eddy onto the variability of these parameters using in situ data from a mooring record. Long-term observations of the temporal variability of energy fluxes of the internal tide are sparse and often with a strong regional focus (Alford et al., 2011; Vic et al., 2018) with few comparisons on the global scale (Ansong et al., 2017). Especially the

interpretation of their interactions with mesoscale flow is often based on theoretical and idealized studies or numerical models (Dunphy & Lamb, 2014; Kerry et al., 2014; Ponte & Klein, 2015; Rainville et al., 2010; Zaron & Egbert, 2014). To our knowledge, the present study is the first where a mooring based observational comparison of the M_2 internal tide energy flux between a distinct eddy and no-eddy phase in the open ocean is performed. This analysis is complemented by comparisons with energy fluxes calculated from the STORMTIDE2 OGCM and energy fluxes derived from satellite altimetry.

The energy fluxes calculated from the measurements and from the STORMTIDE2 model show strong spring-neap variability and are clearly dominated by mode 1. The internal tide measured at the mooring location can directly be assigned to its generation region south of the Azores Islands. The time mean energy fluxes estimated from the measurements of the moored instruments are about 2 times higher compared to those in STORMTIDE2 and the coherent part of the energy flux of the mooring data is about 5 times higher than those inferred from satellite altimetry. Model and observations agree well in the ratio between coherent and incoherent energy flux in the first mode but differ in the coherence of mode 2. The direction of the energy flux is steadily pointing away from the generation site without varying much over time for the mooring time series and STORMTIDE2. All three datasets agree on about 10% of their total energy flux being in mode 2. To conclude, we see a good agreement in the direction of energy flux, the modal composition, and the coherence ratio between mooring measurements, model data and, to some extent, also from satellite altimetry. The latter two, however, are underestimating the total energy flux generated south of the Azores.

Apart from the spring-neap variability, the main temporal variability of the internal tide energy flux is observed during times when eddies pass over the mooring. During the deployment two distinct eddies were passing over the mooring location which allowed us to study the influence of mesoscale motions onto the low-mode internal tide energy flux. We split the time series in three sections, a surface eddy, a subsurface eddy, and a no-eddy time period. Both eddies dampened the energy flux in comparison to the no-eddy period for the semidiurnal component, whereby the subsurface eddy has an almost exclusive effect on the second mode. The damping effect of the eddies on the M_2 coherent part of the energy flux was comparatively stronger than on the total semidiurnal flux, thereby increasing the incoherent part of the total flux. This effect was also more pronounced for the second mode than for the first. The total coherent part of the energy flux is reduced by more than 40% during the surface eddy phase in comparison to the no-eddy period.

Direct measurements of the energy decrease of internal tides away from their generation site provide an important insight on how much energy is available for mixing but their interpretation is challenging due to their temporal and spatial inhomogeneity. We showed that the main temporal variability, beside the spring-neap variability inherent in the forcing, lies in the presence of mesoscale eddies. These eddies do not only influence the temporal variability of the energy flux but also the spatial variability by changing the interference pattern of waves from multiple sources (Dunphy & Lamb, 2014; Rainville et al., 2010; Zaron & Egbert, 2014). Understanding the variability of internal tides is important to interpret sparse observations of ocean mixing and a key factor in improving parameterizations for climate models. Our study supports the role of strong mesoscale variability in transforming the energy of internal tides into mixing (Kerry et al., 2014; Whalen et al., 2012). The mechanism for deep-ocean mixing away from internal tide generation sites, provided by scattering of low-mode internal tide energy to higher modes through interactions with mesoscale eddies, contributes to the spatially varying nonuniform distribution of diapycnal mixing (Simmons et al., 2004; St. Laurent & Simmons, 2006; Walter & Mertens, 2013; Walter et al., 2005; Waterhouse et al., 2014; Whalen et al., 2018).

Coherence is an important factor for the detection of internal tides using satellite altimetry. When internal tides propagate through the ocean, currents, and variations in stratification can modify their phase and group speed and ultimately make them incoherent and create a fictitious energy loss along the propagation path. It is important to improve the separation between true dissipation and loss of coherence to get a better representation of internal tide energy from satellite altimetry. Our findings support the idea that parameterizations of ocean mixing should take also the energy transformation associated with the interaction between internal tides and eddies properly into account, rather than relying mainly on the topographic roughness and pure tidal forcing (Kerry et al., 2014; Liang & Thurnherr, 2012). Few OGCM resolve simultaneously tides and the low-frequency circulation (Arbic et al., 2010; Müller et al., 2012) and adequately predict incoherence of low-mode internal tides. The rareness, cost, and complexity of such realistic models,

as well as observations, limit our understanding of internal tide—eddy interaction and the associated coherence of internal tides. Our study provides a step toward understanding the role of the spatial and temporal variability of internal waves for global ocean mixing estimates.

Data Availability Statement

This study has been conducted using E.U. Copernicus Marine Service Information providing the CMEMS SSH dataset (http://marine.copernicus.eu/services-portfolio/access-to-products/?option=com_csw&view=details&product_id=SEALEVEL_GLO_PHY_L4_REP_OBSERVATIONS_008_047). A subset of this dataset was downloaded on November 20, 2018. The TPXO9 model was downloaded on March 7, 2018 (https://www.tpxo.net/global) and is available upon request. The mooring data is available under https://doi.org/10.1594/PANGAEA.918730. The data from the STORMTIDE2 model is available upon request and will be submitted to Pangaea data repository. The energy fluxes derived from satellite altimetry are available under https://doi.org/10.6084/m9.figshare.8316956 for mode 1 and https://doi.org/10.6084/m9.figshare.7116836 for mode 2.

Acknowledgments
This study is a contribution to the project W2 (Energy transfers through low-mode internal waves) of the Collaborative Research Centre TRR 181 "Energy Transfer in Atmosphere and Ocean" funded by the Deutsche Forschungsgemeinschaft (DFG, German Research Foundation)—Project number 274762653. We furthermore want to thank Dirk Olbers for helpful discussions. Open access funding enabled and organized by Projekt DEAL

References

Alford, M. H. (2003). Redistribution of energy available for ocean mixing by long-range propagation of internal waves. *Nature*, *423*, 159. https://doi.org/10.1038/nature01628

Alford, M. H., MacKinnon, J. A., Nash, J. D., Simmons, H., Pickering, A., Klymak, J. M., et al. (2011). Energy flux and dissipation in Luzon Strait: Two tales of two ridges. *Journal of Physical Oceanography*, *41*(11), 2211–2222. https://doi.org/10.1175/jpo-d-11-073.1

Alford, M. H., Mickett, J. B., Zhang, S., MacCready, P., Zhao, Z., & Newton, J. (2012). Internal waves on the Washington continental shelf. *Oceanography*, *25*, 66–79. https://doi.org/10.5670/oceanog.2012.43

Alford, M. H., & Zhao, Z. (2007). Global patterns of low-mode internal-wave propagation. Part I: Energy and energy flux. *Journal of Physical Oceanography*, *37*(7), 1829–1848. https://doi.org/10.1175/jpo3085.1

Anderson, D. L. T., & Gill, A. E. (1979). Beta dispersion of inertial waves. *Journal of Geophysical Research*, *84*(C4), 1836–1842. https://doi.org/10.1029/JC084iC04p01836

Ansong, J. K., Arbic, B. K., Alford, M. H., Buijsman, M. C., Shriver, J. F., Zhao, Z., et al. (2017). Semidiurnal internal tide energy fluxes and their variability in a Global Ocean Model and moored observations. *Journal of Geophysical Research: Oceans*, *122*(3), 1882–1900. https://doi.org/10.1002/2016JC012184

Arbic, B. K., Richman, J. G., Shriver, J. F., Timko, P. G., Metzger, E. J., & Wallcraft, A. J. (2012). Global modeling of internal tides within an eddying ocean general circulation model. *Oceanography*, *25*, 20–29. https://doi.org/10.5670/oceanog.2012.38

Arbic, B. K., Wallcraft, A. J., & Metzger, E. J. (2010). Concurrent simulation of the eddying general circulation and tides in a global ocean model. *Ocean Modelling*, *32*(3), 175–187. https://doi.org/10.1016/j.ocemod.2010.01.007

Buijsman, M. C., Ansong, J. K., Arbic, B. K., Richman, J. G., Shriver, J. F., Timko, P. G., et al. (2016). Impact of parameterized internal wave drag on the semidiurnal energy balance in a global ocean circulation model*. *Journal of Physical Oceanography*, *46*(5), 1399–1419. https://doi.org/10.1175/jpo-d-15-0074.1

Chavanne, C., Flament, P., Luther, D., & Gurgel, K.-W. (2010). The surface expression of semidiurnal internal tides near a strong source at Hawaii. Part II: Interactions with mesoscale currents. *Journal of Physical Oceanography*, *40*(6), 1180–1200. https://doi.org/10.1175/2010jpo4223.1

Cummins, P. F., Cherniawsky, J. Y., & Foreman, M. G. G. (2001). North Pacific internal tides from the Aleutian Ridge: Altimeter observations and modeling. *Journal of Marine Research*, *59*(2), 167–191. https://doi.org/10.1357/002224001762882628

de Lavergne, C., Falahat, S., Madec, G., Roquet, F., Nycander, J., & Vic, C. (2019). Toward global maps of internal tide energy sinks. *Ocean Modelling*, *137*, 52–75. https://doi.org/10.1016/j.ocemod.2019.03.010

Dunphy, M., & Lamb, K. G. (2014). Focusing and vertical mode scattering of the first mode internal tide by mesoscale eddy interaction. *Journal of Geophysical Research: Oceans*, *119*(1), 523–536. https://doi.org/10.1002/2013jc009293

Dunphy, M., Ponte, A. L., Klein, P., & Gentil, S. L. (2017). Low-mode internal tide propagation in a turbulent eddy field. *Journal of Physical Oceanography*, *47*(3), 649–665. https://doi.org/10.1175/jpo-d-16-0099.1

Dushaw, B. D., Howe, B. M., Cornuelle, B. D., Worcester, P. F., & Luther, D. S. (1995). Barotropic and baroclinic tides in the central North Pacific Ocean determined from long-range reciprocal acoustic transmissions. *Journal of Physical Oceanography*, *25*(4), 631–647. https://doi.org/10.1175/1520-0485(1995)025<0631:Babtit>2.0.Co;2

Eden, C. (2007). Eddy length scales in the North Atlantic Ocean. *Journal of Geophysical Research*, *112*(C6). https://doi.org/10.1029/2006jc003901

Eden, C., Czeschel, L., & Olbers, D. (2014). Toward energetically consistent ocean models. *Journal of Physical Oceanography*, *44*(12), 3160–3184. https://doi.org/10.1175/jpo-d-13-0260.1

Egbert, G. D., & Erofeeva, S. Y. (2002). Efficient inverse modeling of barotropic ocean tides. *Journal of Atmospheric and Oceanic Technology*, *19*(2), 183–204. https://doi.org/10.1175/1520-0426(2002)019<0183:Eimobo>2.0.Co;2

Fischer, J., & Visbeck, M. (1993). Seasonal variation of the daily zooplankton migration in the Greenland Sea. *Deep Sea Research Part I: Oceanographic Research Papers*, *40*(8), 1547–1557. https://doi.org/10.1016/0967-0637(93)90015-U

Haji, M. N. (2015). *Scattering of the low-mode internal tide at the Line Islands Ridge* (Master thesis). Cambridge, MA: Massachusetts Institute of Technology. http://hdl.handle.net/1721.1/97852C

Kelly, S. M., & Lermusiaux, P. F. J. (2016). Internal-tide interactions with the Gulf stream and middle Atlantic bight shelfbreak front. *Journal of Geophysical Research: Oceans*, *121*(8), 6271–6294. https://doi.org/10.1002/2016jc011639

Kelly, S. M., Lermusiaux, P. F. J., Duda, T. F., & Haley, P. J., Jr. (2016). A coupled-mode shallow-water model for tidal analysis: Internal tide reflection and refraction by the Gulf stream. *Journal of Physical Oceanography*, *46*(12), 3661–3679. https://doi.org/10.1175/jpo-d-16-0018.1

Kelly, S. M., & Nash, J. D. (2010). Internal-tide generation and destruction by shoaling internal tides. *Geophysical Research Letters*, *37*(23). https://doi.org/10.1029/2010gl045598

Kerry, C. G., Powell, B. S., & Carter, G. S. (2014). The impact of subtidal circulation on internal-tide-induced mixing in the Philippine Sea. *Journal of Physical Oceanography*, *44*(12), 3209–3224. https://doi.org/10.1175/jpo-d-13-0249.1

Köhler, J., Walter, M., Mertens, C., Stiehler, J., Li, Z., Zhao, Z., et al. (2019). Energy flux observations in an internal tide beam in the eastern North Atlantic. *Journal of Geophysical Research: Oceans*, *124*(8), 5747–5764. https://doi.org/10.1029/2019jc015156

Krauss, W., Döscher, R., Lehmann, A., & Viehoff, T. (1990). On eddy scales in the eastern and northern North Atlantic Ocean as a function of latitude. *Journal of Geophysical Research*, *95*(C10), 18049–18056. https://doi.org/10.1029/JC095iC10p18049

Kunze, E., Rosenfeld, L. K., Carter, G. S., & Gregg, M. C. (2002). Internal waves in Monterey submarine canyon. *Journal of Physical Oceanography*, *32*(6), 1890–1913. https://doi.org/10.1175/1520-0485(2002)032<1890:Iwimsc>2.0.Co;2

Liang, X., & Thurnherr, A. M. (2012). Eddy-modulated internal waves and mixing on a Midocean Ridge. *Journal of Physical Oceanography*, *42*(7), 1242–1248. https://doi.org/10.1175/jpo-d-11-0126.1

Li, Q., Mao, X., Huthnance, J., Cai, S., & Kelly, S. (2019). On internal waves propagating across a geostrophic front. *Journal of Physical Oceanography*, *49*(5), 1229–1248. https://doi.org/10.1175/jpo-d-18-0056.1

Li, Z., von Storch, J. S., & Müller, M. (2015). The M2 internal tide simulated by a 1/10° OGCM. *Journal of Physical Oceanography*, *45*(12), 3119–3135. https://doi.org/10.1175/jpo-d-14-0228.1

Li, Z., von Storch, J.-S., & Müller, M. (2017). The K1 internal tide simulated by a 1/10° OGCM. *Ocean Modelling*, *113*, 145–156. https://doi.org/10.1016/j.ocemod.2017.04.002

MacKinnon, J. A., Zhao, Z., Whalen, C. B., Waterhouse, A. F., Trossman, D. S., Sun, O. M., et al. (2017). Climate process team on internal wave–driven ocean mixing. *Bulletin of the American Meteorological Society*, *98*(11), 2429–2454. https://doi.org/10.1175/bams-d-16-0030.1

McWilliams, J. C. (1985). Submesoscale, coherent vortices in the ocean. *Reviews of Geophysics*, *23*(2), 165–182. https://doi.org/10.1029/RG023i002p00165

Müller, M., Cherniawsky, J. Y., Foreman, M. G. G., & von Storch, J. S. (2012). Global M2 internal tide and its seasonal variability from high resolution ocean circulation and tide modeling. *Geophysical Research Letters*, *39*(19). https://doi.org/10.1029/2012gl053320

Munk, W., & Wunsch, C. (1998). Abyssal recipes II: Energetics of tidal and wind mixing. *Deep Sea Research Part I: Oceanographic Research Papers*, *45*(12), 1977–2010. https://doi.org/10.1016/S0967-0637(98)00070-3

Nash, J. D., Alford, M. H., & Kunze, E. (2005). Estimating internal wave energy fluxes in the ocean. *Journal of Atmospheric and Oceanic Technology*, *22*(10), 1551–1570. https://doi.org/10.1175/jtech1784.1

Nash, J. D., Kelly, S. M., Shroyer, E. L., Moum, J. N., & Duda, T. F. (2012). The unpredictable nature of internal tides on continental shelves. *Journal of Physical Oceanography*, *42*(11), 1981–2000. https://doi.org/10.1175/jpo-d-12-028.1

Nash, J. D., Kunze, E., Toole, J. M., & Schmitt, R. W. (2004). Internal tide reflection and turbulent mixing on the continental slope. *Journal of Physical Oceanography*, *34*(5), 1117–1134. https://doi.org/10.1175/1520-0485(2004)034<1117:Itratm>2.0.Co;2

Nash, J. D., Shroyer, E. L., Kelly, S. M., Inall, M. E., Duda, T. F., Levine, M. D., et al. (2012). Are any coastal internal tides predictable? *Oceanography*, *25*. https://doi.org/10.5670/oceanog.2012.44

Nycander, J. (2005). Generation of internal waves in the deep ocean by tides. *Journal of Geophysical Research*, *110*(C10). https://doi.org/10.1029/2004jc002487

Pawlowicz, R., Beardsley, B., & Lentz, S. (2002). Classical tidal harmonic analysis including error estimates in MATLAB using T_TIDE. *Computers & Geosciences*, *28*(8), 929–937. https://doi.org/10.1016/S0098-3004(02)00013-4

Ponte, A. L., & Klein, P. (2015). Incoherent signature of internal tides on sea level in idealized numerical simulations. *Geophysical Research Letters*, *42*(5), 1520–1526. https://doi.org/10.1002/2014GL062583

Rainville, L., Johnston, T. M. S., Carter, G. S., Merrifield, M. A., Pinkel, R., Worcester, P. F., & Dushaw, B. D. (2010). Interference pattern and propagation of the M2 internal tide south of the Hawaiian Ridge. *Journal of Physical Oceanography*, *40*(2), 311–325. https://doi.org/10.1175/2009jpo4256.1

Rainville, L., & Pinkel, R. (2006). Propagation of low-mode internal waves through the ocean. *Journal of Physical Oceanography*, *36*(6), 1220–1236. https://doi.org/10.1175/jpo2889.1

Ray, R. D., & Zaron, E. D. (2011). Non-stationary internal tides observed with satellite altimetry. *Geophysical Research Letters*, *38*(17). https://doi.org/10.1029/2011gl048617

Richman, J. G., Arbic, B. K., Shriver, J. F., Metzger, E. J., & Wallcraft, A. J. (2012). Inferring dynamics from the wavenumber spectra of an eddying global ocean model with embedded tides. *Journal of Geophysical Research*, *117*(C12). https://doi.org/10.1029/2012jc008364

Saidi, J. S. (2011). *Experimental investigation of 2D and 3D internal wave fields* (Master thesis). Cambridge, MA: Massachusetts Institute of Technology. http://hdl.handle.net/1721.1/67799

Savage, A. C., Arbic, B. K., Alford, M. H., Ansong, J. K., Farrar, J. T., Menemenlis, D., et al. (2017). Spectral decomposition of internal gravity wave sea surface height in global models. *Journal of Geophysical Research: Oceans*, *122*(10), 7803–7821. https://doi.org/10.1002/2017jc013009

Shriver, J. F., Richman, J. G., & Arbic, B. K. (2014). How stationary are the internal tides in a high-resolution global ocean circulation model? *Journal of Geophysical Research: Oceans*, *119*(5), 2769–2787. https://doi.org/10.1002/2013jc009423

Simmons, H. L., & Alford, M. H. (2012). Simulating the long-range swell of internal waves generated by ocean storms. *Oceanography*, *25*(2), 30–41. https://doi.org/10.5670/oceanog.2012.39

Simmons, H. L., Jayne, S. R., Laurent, L. C. S., & Weaver, A. J. (2004). Tidally driven mixing in a numerical model of the ocean general circulation. *Ocean Modelling*, *6*(3), 245–263. https://doi.org/10.1016/S1463-5003(03)00011-8

St. Laurent, L., & Garrett, C. (2002). The role of internal tides in mixing the deep ocean. *Journal of Physical Oceanography*, *32*(10), 2882–2899. https://doi.org/10.1175/1520-0485(2002)032<2882:Troiti>2.0.Co;2

St. Laurent, L., & Simmons, H. (2006). Estimates of power consumed by mixing in the ocean interior. *Journal of Climate*, *19*(19), 4877–4890. https://doi.org/10.1175/jcli3887.1

Vic, C., Garabato, A. C. N., Green, J. A. M., Spingys, C., Forryan, A., Zhao, Z., & Sharples, J. (2018). The lifecycle of semidiurnal internal tides over the Northern mid-Atlantic Ridge. *Journal of Physical Oceanography*, *48*(1), 61–80. https://doi.org/10.1175/jpo-d-17-0121.1

Walter, M., Köhler, J., Löb, J., Sukjikh, N., Böke, W., Münzner, F., & Rümmler, S. (2018). *RV POSEIDON 516 [POS516] Cruise Report/Fahrtbericht, Ponta Delgada (Azores) 29.07.2017—Ponta Delgada (Azores) 18.08.2017, POS516–ENERGY TRANSFER*. Zentrum für Marine Umweltwissenschaften, Universität Bremen. https://doi.org/10.3289/CR_POS516

Walter, M., & Mertens, C. (2013). Mid-depth mixing linked to North Atlantic current variability. *Geophysical Research Letters*, *40*(18), 4869–4875. https://doi.org/10.1002/grl.50936

Walter, M., Mertens, C., & Rhein, M. (2005). Mixing estimates from a large-scale hydrographic survey in the North Atlantic. *Geophysical Research Letters*, *32*(13). https://doi.org/10.1029/2005gl022471

Waterhouse, A. F., MacKinnon, J. A., Nash, J. D., Alford, M. H., Kunze, E., Simmons, H. L., et al. (2014). Global patterns of diapycnal mixing from measurements of the turbulent dissipation rate. *Journal of Physical Oceanography*, *44*(7), 1854–1872. https://doi.org/10.1175/jpo-d-13-0104.1

Whalen, C. B., MacKinnon, J. A., & Talley, L. D. (2018). Large-scale impacts of the mesoscale environment on mixing from wind-driven internal waves. *Nature Geoscience*, *11*(11), 842–847. https://doi.org/10.1038/s41561-018-0213-6

Whalen, C. B., Talley, L. D., & MacKinnon, J. A. (2012). Spatial and temporal variability of global ocean mixing inferred from Argo profiles. *Geophysical Research Letters*, *39*(18). https://doi.org/10.1029/2012gl053196

Wunsch, C., & Ferrari, R. (2004). Vertical mixing, energy, and the general circulation of the oceans. *Annual Review of Fluid Mechanics*, *36*(1), 281–314. https://doi.org/10.1146/annurev.fluid.36.050802.122121

Zaron, E. D., & Egbert, G. D. (2014). Time-variable refraction of the internal tide at the Hawaiian Ridge. *Journal of Physical Oceanography*, *44*(2), 538–557. https://doi.org/10.1175/jpo-d-12-0238.1

Zhao, Z. (2018). The global mode-2 M2 internal tide. *Journal of Geophysical Research: Oceans*, *123*(11), 7725–7746. https://doi.org/10.1029/2018JC014475

Zhao, Z., Alford, M. H., Girton, J. B., Rainville, L., & Simmons, H. L. (2016). Global observations of open-ocean mode-1 M2 internal tides. *Journal of Physical Oceanography*, *46*(6), 1657–1684. https://doi.org/10.1175/jpo-d-15-0105.1

Zhao, Z., Alford, M. H., MacKinnon, J. A., & Pinkel, R. (2010). Long-Range propagation of the semidiurnal internal tide from the Hawaiian Ridge. *Journal of Physical Oceanography*, *40*(4), 713–736. https://doi.org/10.1175/2009jpo4207.1

Zilberman, N. V., Merrifield, M. A., Carter, G. S., Luther, D. S., Levine, M. D., & Boyd, T. J. (2011). Incoherent nature of M2 internal tides at the Hawaiian Ridge. *Journal of Physical Oceanography*, *41*(11), 2021–2036. https://doi.org/10.1175/jpo-d-10-05009.1